



Freestanding catalytic membranes assembled from blade-shaped Prussian blue analog sheets for flow-through degradation of antibiotic pollutants

Jiaxin Li^a, Huiyu Yi^a, Yang Xiao^c, Cheng Liang^a, Yi Shen^d, Yungui Li^e, Qile Fang^{a,b,*}

^a Research and Development Center for Watershed Environmental Eco-Engineering, Beijing Normal University, Zhuhai 519087, PR China

^b State Key Laboratory of Water Environment Simulation, School of Environment, Beijing Normal University, Beijing 100875, PR China

^c School of Civil Engineering, Wuhan University, Wuhan 430072, PR China

^d Key Laboratory of Microbial Technology for Industrial Pollution Control of Zhejiang Province, College of Environment, Zhejiang University of Technology, Hangzhou 310032, PR China

^e Sichuan Provincial Sci-Tech Cooperation Base of Low-cost Wastewater Treatment Technology, Department of Environmental Engineering, Southwest University of Science and Technology, Mianyang 621010, PR China

ARTICLE INFO

Keywords:

Catalytic membrane
Prussian blue analog sheets
Instantaneous degradation
Antibiotic pollutant

ABSTRACT

Membrane catalysis is a frontier technology for effectively removing organic contaminants, and burgeoning membranes assembled from two-dimensional (2D) materials have significantly flourished in peroxymonosulfate (PMS)-based catalytic membrane processes. Here, a bottom-up strategy based on restricting CoFe Prussian blue analog (PBA) crystal growth in one direction is used to fabricate large-scale 2D blade-shaped PBA sheets, whose radial size and thickness can be adjusted by the precursor ion ratio ($\text{Co}^{II}/\text{Fe}^{II}$). The stripe CoFe PBA sheets can directly serve as building blocks and are simply assembled into a free-standing 2D membrane by interweaving assembly. The assembled CoFe PBA catalytic membrane possesses excellent wetting properties, guaranteeing an unimpeded mass transfer process, which leads to a superior instantaneous catalytic performance for the antibiotic norfloxacin during the continuous and flow-through membrane catalytic process. $\text{SO}_4^{\bullet-}$ and $^1\text{O}_2$ are demonstrated to be the main active species, which synergistically contribute to the PMS-driven organic degradation.

1. Introduction

Antibiotic contamination has been frequently detected in drinking water sources, natural waters and sewage treatment plant effluents at levels that can jeopardize public or ecosystem health (including toxic effects and antibiotic resistance) [1,2]. Traditional water treatment processes such as coagulation, flocculation and biological methods have been reported to be ineffective or insufficient for the removal of such emerging contaminants [3]. This fact underscores the need for technological innovation to achieve effective decontamination, and heterogeneous catalysis is a highly promising solution for stubborn antibiotic contaminants, which involves the use of an advanced oxidation process (AOP) to generate reactive oxygen species to attack organic contaminants [4,5].

In recent years, the integration of membrane filtration and AOPs has progressively gained extensive attention for organic contaminant

degradation, i.e., catalytic membrane technology [6,7]. The catalytic membrane represents a localization of micro/nano catalyst particles within a macroscopic membrane body, which can properly overcome the main challenges faced in powder catalyst applications for water treatment: i) the catalytic membrane can avoid the difficulty of separation and recovery of catalyst particles from the treated solution [8]; ii) the catalytic membrane can effectively prevent catalyst passivation during the catalysis process due to its continuous dynamic running process involving the fresh input of target pollutants/oxidants and the prompt output of degradation products [9]; iii) the catalytic membrane provides numerous microreactors in its membrane pores, which can largely narrow the concentration boundary layer for organic pollutant diffusion and can greatly promote the utilization of reactive oxygen species [10,11]. Thus, catalytic membrane technology as a dynamic AOP process is considered to be a frontier technology for the effective removal of organic contaminants in wastewater treatment. Currently,

* Corresponding author at: Research and Development Center for Watershed Environmental Eco-Engineering, Beijing Normal University, Zhuhai 519087, PR China.

E-mail address: fangqile@bnu.edu.cn (Q. Fang).

<https://doi.org/10.1016/j.apcatb.2023.122922>

Received 31 March 2023; Received in revised form 26 April 2023; Accepted 25 May 2023

Available online 26 May 2023

0926-3373/© 2023 Elsevier B.V. All rights reserved.

peroxymonosulfate (PMS)-based AOPs have drawn more attention to be coupled in the catalytic membrane process for dynamic organic degradation given their higher reactivity, higher stability, higher yield of radical formation, and higher redox potential than H_2O_2 -based AOPs [12,13].

Burgeoning membranes assembled from one-dimensional (1D) or two-dimensional (2D) nanomaterials have significantly flourished in PMS-based catalytic membrane technology, considering their exceptional nanoconfinement effect and high structure designability [14–17]. In particular, the 2D nanosheet-assembled lamellar catalytic membrane possesses highly accessible active sites on the sheet surfaces when flowing through the interlayer mass transfer channels [18,19]. Chen et al. reported a lamellar catalytic membrane assembled from 2D MoS_2 nanosheets, whose nanolayers with nonlinear transport enabled high yields and efficient utilization of instantaneously produced free radicals [14]. In addition, several types of other 2D nanomaterials have been developed to construct lamellar catalytic membranes, such as Co-Cu oxide nanosheets [15], Co-TiOx nanosheets [13], and CoAl-layered double hydroxide nanosheets [20], where the 2D nanosheets perform two functions: i) building blocks for 2D membrane assembly and ii) active catalysts for organic contamination degradation. Only the 2D building block with a certain length-diameter ratio can be used to construct lamellar membranes, and the current way to synthesize 2D nanosheets with catalytic activity mainly relies on the top-down method involving exfoliation from the bulk materials [21–23], which suffers from the problems of inhomogeneity, low yield, fragmentation and restacking of the detached sheets [24]. On the other hand, layered bulk materials (usually those containing transition metals) with catalytic activity are usually prepared under extreme high-temperature or high-pressure conditions, which largely restricts their mass production and application. Therefore, for the construction of 2D catalytic membranes, the large-scale synthesis of 2D catalytic-active building blocks with morphological uniformity, structural integrity, higher yield and an environmentally friendly approach remains a great challenge [25].

Prussian blue analogs (PBAs) with the chemical formula of $\text{A}_x\text{M}[\text{M}'(\text{CN})_6]_y \cdot n\text{H}_2\text{O}$ (A, alkaline metal; M and M', transition metal ions; \square , $[\text{M}'(\text{CN})_6]$ vacancies occupied by coordinated water; $0 \leq x \leq 2$, $0 \leq y \leq 1$) [26] have been reported to a class of superior catalysts for organic contamination degradation [27–30]. The coordination of divalent metal of M (including Fe^{II} , Co^{II} , Mn^{II} , Zn^{II} , Mn^{II} , et al.) and trivalent metal of M' (including Fe^{III} , Co^{III} , et al.) usually results in a variety of PBAs with different morphologies and catalytic properties [31,32]. In this work, a bottom-up strategy was conducted to fabricate large-scale 2D blade-shape CoFe PBA sheets by adjusting two divalent metal ions ratio ($\text{Co}^{\text{II}}/\text{Fe}^{\text{II}}$) and restricting the growth of the coordination polymer in one direction at room temperature, which in turn can be directly assembled into a freestanding 2D catalytic membrane without any exfoliation step. The assembled CoFe PBA catalytic membrane was successfully used for the dynamic degradation of the antibiotic norfloxacin (NOR) in a flow-through running mode. The catalytic membrane performances, including flux and removal, were evaluated under varying operating pressure, 2D sheet content and PMS dosage. Reactive radical trapping and quenching tests were performed to research the membrane catalytic mechanism for antibiotic degradation.

2. Experimental section

2.1. Chemicals

$\text{Na}_4\text{Fe}(\text{CN})_6 \cdot 10 \text{H}_2\text{O}$ and $\text{CoSO}_4 \cdot 7 \text{H}_2\text{O}$ were purchased from Shanghai Aladdin Biochemical Technology Co. Ltd. Potassium persulfate (PMS, 42–46 % KHSO_5), norfloxacin (NOR, 98 %), L-histidine (≥ 99.0 %) and tert-butanol (TBA, ≥ 99.0 %) were supplied by Shanghai Macklin Biochemical Co. Ltd. Methanolic acid (HPLC) and methanol (MeOH, ≥ 99.9 %) were received from ANPEL Laboratory Technologies (Shanghai) Inc. CA-CN mixed fiber microporous filter membranes (0.22

μm) were purchased from Haiyan New Oriental Plastic & Chemical Technology Co. Ltd. Deionized water (18 $\text{M}\Omega/\text{cm}$) was used in all experiments. All the materials were used without any further treatment.

2.2. Preparation of CoFe PBA sheets and catalytic membrane

CoFe PBA sheets were synthesized by a controlled coordination polymerization method. Then, 500 mL of 4 mM CoSO_4 solution was prepared, and 100 mL of $\text{Na}_4\text{Fe}(\text{CN})_6$ solution with different concentrations (from 1 mM to 12 mM) was added into the CoSO_4 solution by strictly controlling the addition speed (5 mL/min) using a peristaltic pump. A green precipitate was observed to form immediately, and the mixture was vigorously stirred at room temperature. After 20 min of supply, the stirring was stopped, and the mixture was allowed to stand for another 12 h to achieve a complete coordination reaction. Then, the solid product was collected by filtration and washed 2–3 times with deionized (DI) water. The final product was obtained after vacuum-drying at 60 °C. Depending on the concentration of sodium ferrocyanide, the samples were labeled CoFe PBAs-1, CoFe PBAs-2, CoFe PBAs-4, etc., according to the concentration of the $\text{Na}_4\text{Fe}(\text{CN})_6$ solution used in the fabrication process.

A method of gas-pressing filtration was used to prepare CoFe PBA catalytic membranes, and the detailed process is as follows: weight CoFe PBA powders of different quality and add it into 50 mL DI water to form a uniform dispersion under a 2 min ultrasound-assisted process. The dispersion was then injected into a homemade cell by N_2 -pressing filtration using 0.22 μm mixed cellulose membrane as the substrate membrane. Subsequently, the CoFe PBAs sheets were assembled into a free-standing membrane after natural drying.

2.3. Characterization

Scanning electron microscopy (SEM, Hitachi, S4800, Japan), transmission electron microscopy (TEM, FEI, Tecnai F20, US) equipped with energy dispersive spectroscopy (EDS, Smartedx) and atomic force microscopy (AFM, Bruker, Dimension Icon, Germany) were used to characterize the morphological features and elemental distribution of the prepared samples. The specific surface area was tested by using the Brunauer–Emmett–Teller (BET) method for N_2 adsorption/desorption measured with a surface area analyzer (Micromeritics, ASAP2460, US). X-ray diffraction (XRD) patterns were obtained using a diffractometer (Rigaku, Ultima VI, Japan). X-ray photoelectron spectroscopy (XPS, Kratos, Axis Ultra DLD, Japan) was used to analyze the chemical composition of the samples. The water contact angle in air (CA, OCA100, Dataphysics, Germany) was used to assess the surface wettability of the prepared 2D membranes. Electron paramagnetic resonance (EPR, Bruker, EMXnano, Germany) was used to detect the active radical signals. The identification of NOR and its degradation products was performed on an ultrahigh-performance liquid chromatography coupled with quadrupole-time of flight mass spectrometry (UPLC-Q-TOF, Agilent, 1290–6546, US).

2.4. Catalytic membrane performance for NOR degradation

Norfloxacin (NOR) was selected as the representative antibiotic contaminant in this work to evaluate the performance of the powder catalysts and 2D catalytic membranes. For the powder catalysis test, 10 mg of catalyst was dispersed into 100 mL NOR aqueous solution (10 mg L^{-1}) and stirred for 0.5 h to achieve an apparent adsorption equilibrium. Then, 5 mg of PMS was added to trigger the oxidation reaction, and the solution was collected at different time intervals followed by filtration using 0.22 μm membrane and an immediate quenching using methanol. Then, the NOR concentration was monitored using ultrahigh-performance liquid chromatography–mass spectrometry (UPLC–MS, Waters, XEVO TQ-XS, US). For the dynamic membrane catalysis test, a homemade gas-pressing filtration setup was used to evaluate the

catalytic efficiency and permeation of the as-prepared 2D CoFe PBA membranes. The removal efficiency R (%) was calculated as follows:

$$R(\%) = \frac{C_{\text{NOR}} - C_{\text{S}}}{C_{\text{NOR}}} \times 100\% \quad (1)$$

where R is the removal rate and C_{NOR} and C_{S} are the initial and real-time concentrations of NOR during the degradation process, respectively.

The membrane flux was calculated using the following equation:

$$J = \frac{V}{t \times A}$$

where J is the flux ($\text{L m}^{-2}\text{h}^{-1}$), V (L) is the 2D membrane permeation volume of water, A (m^2) is the effective filtration area of the 2D CoFe PBA membrane and t (h) is the experimental time.

3. Results and discussion

3.1. Morphology and structure of CoFe PBA sheets

A bottom-up strategy under room temperature conditions was used for the large-scale fabrication of 2D catalytic building blocks in this work. As described in Fig. 1a, strict control of the $\text{Co}^{\text{II}}/\text{Fe}^{\text{II}}$ ratio and supply rate was adopted to guide the orientated growth of Prussian

white crystals (a reduced form of PBA) [33–35]. First, an obvious Tyndal effect (Fig. 1b) and liquid crystal phenomenon (Fig. 1c, Video S1) can be observed on the CoFe PBA solution at low and high concentrations, respectively, which apparently supports the homogeneity and ordering of the fabricated building blocks. In particular, the lyotropic liquid crystal phenomenon that occurs at high concentrations of PBA solution demonstrates a long-range ordered arrangement of CoFe PBA blocks in aqueous solution that usually occurs on one-dimensional or two-dimensional nanomaterials with a large aspect ratio (or width/thickness ratio) and sufficient dispersibility/solubility, such as graphene oxides [36,37]. More clearly, homogeneous blade-shaped 2D sheets can be observed in the SEM images of the CoFe PBA samples shown in Fig. 1d-i. The $\text{Co}^{\text{II}}/\text{Fe}^{\text{II}}$ ratio is an essential factor for the successful fabrication of CoFe PBAs with a 2D sheet structure, and only the use of a $\text{Co}^{\text{II}}/\text{Fe}^{\text{II}}$ ratio above 5 (so that is CoFe PBAs-4) can lead to formation of a distinct sheet structure, while samples with a low $\text{Co}^{\text{II}}/\text{Fe}^{\text{II}}$ ratio (i.e., CoFe PBAs-6, CoFe PBAs-8 and CoFe PBAs-12) are irregular in shape (Fig. S1). Within the threshold range of the $\text{Co}^{\text{II}}/\text{Fe}^{\text{II}}$ ratio, Fig. 1g-i show that a higher $\text{Co}^{\text{II}}/\text{Fe}^{\text{II}}$ ratio (with less Fe^{II} supply) leads to a smaller sheet size for the CoFe PBAs ($\text{CoFe PBAs-1} < \text{CoFe PBAs-2} < \text{CoFe PBAs-4}$). In addition, the supply rate of $\text{Fe}(\text{CN})_6^{4-}$ to coordinate with Co^{II} is important for the integrity of CoFe PBA sheets, and too fast a supply of $\text{Fe}(\text{CN})_6^{4-}$ can result in a large amount of small debris (Fig. S2); thus, strict control of the coordination ion supply at a low speed of 5 mL/min was used in

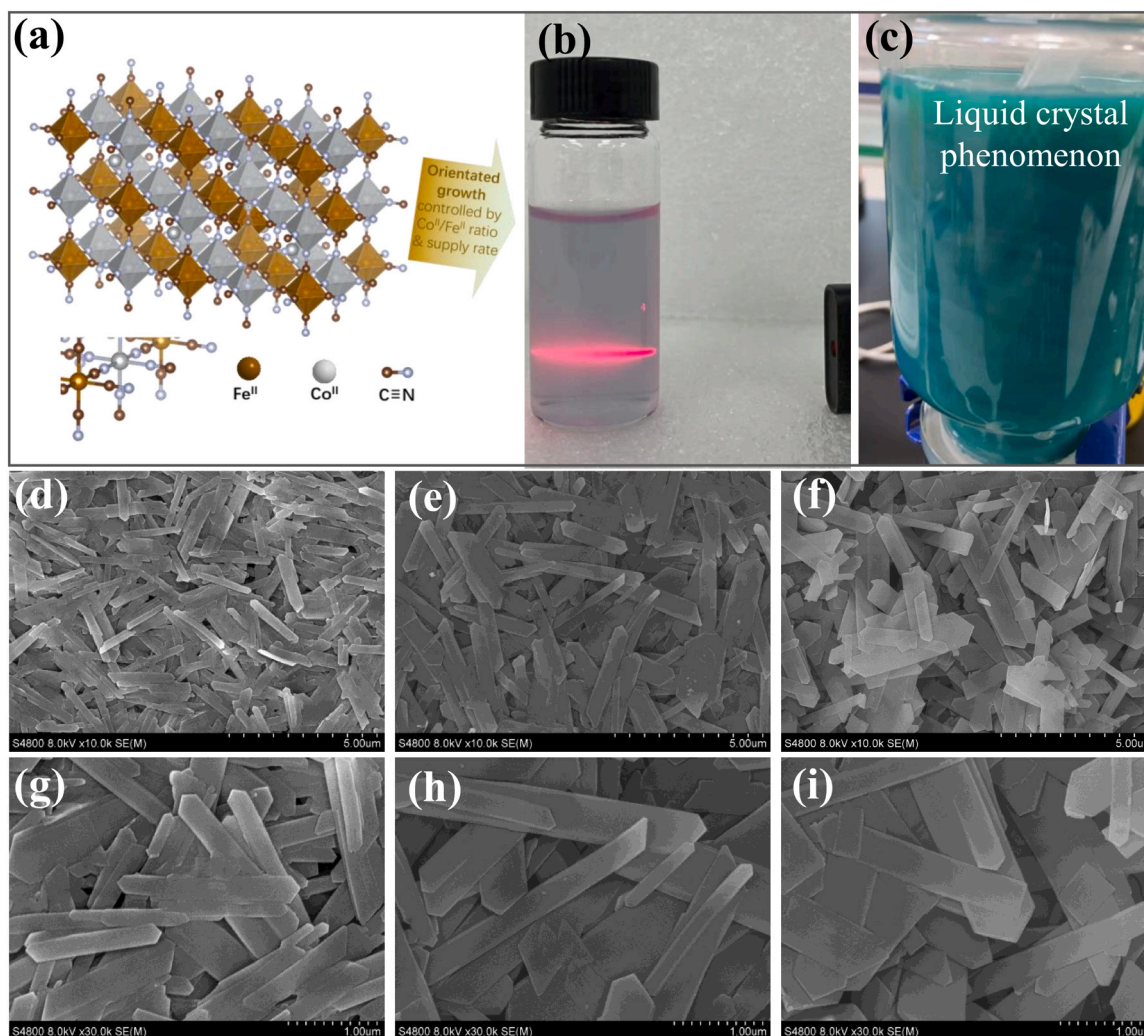


Fig. 1. (a) Structure diagram of CoFe PBA with oriented growth under controlled coordination polymerization; (b) Tyndal phenomenon for CoFe PBA dispersed in an aqueous solution; (c) Liquid crystal phenomenon for CoFe PBA with high concentrations; SEM images of CoFe PBAs-1 (d, g), CoFe PBAs-2 (e, h), and CoFe PBAs-4 (f, i).

this study to obtain complete 2D CoFe PBA sheets.

TEM and AFM were further conducted to study the 2D morphology of CoFe PBA sheets, as shown in Fig. 2. A lamellar structure of the blade-shaped sheets with a small thickness and uniform element distribution can be verified by TEM images and EDS, where the amorphous dispersion rings detected in the SAED pattern (Fig. 2d) illustrate an amorphous state or low degree of crystallinity of the as-prepared CoFe PBAs. Without any exfoliation process, the thickness of the CoFe PBAs-1 sheet is measured to be ~ 85 nm (Fig. 2f), and a lower $\text{Co}^{\text{II}}/\text{Fe}^{\text{II}}$ ratio not only leads to a larger sheet size but also a higher lamellar thickness of the CoFe PBA, as shown by the increase in the thickness of CoFe PBAs-2 (150 nm) and CoFe PBAs-4 (300 nm), respectively (Fig. 2h). Therefore, the large width/thickness ratio of the sheets enables the lyotropic liquid crystal phenomenon, as displayed in Fig. 1c. During the orientated growth process of 2D PBA sheets, it can be thought that the kinetics and thermodynamics of PBA polymerization are the two guarantees for the successful synthesis of coordination compounds under normal pressure and temperature in this study [38], and the facile, green and low-energy

preparation method enables the large-scale synthesis of CoFe PBA sheets, facilitating its application as catalyst or building blocks of catalytic membrane.

The N_2 adsorption-desorption curves shown in Fig. 3a reveal that CoFe PBAs-1 with the smallest radial dimension and the thinnest lamellar possess the highest specific surface area ($45 \text{ m}^2/\text{g}$), which is attributed to the higher content of micropores ($< 2 \text{ nm}$) and mesopores ($4\text{--}50 \text{ nm}$), as displayed by the pore distribution curves in the inset diagram of Fig. 3a, while the thicker CoFe PBAs-2 and CoFe PBAs-4 sheets with larger sheet sizes show lower specific surface areas ($25 \text{ m}^2/\text{g}$). The low $\text{Fe}(\text{CN})_6^{\text{IV}}$ supply for coordination with Co^{II} (excessive) in the rapid coordination polymerization system of CoFe PBAs-1 leads to the creation of more crystal defects and then more micro/mesopores in its 2D crystal structure. The weak diffraction peaks observed in the XRD patterns shown in Fig. 3b also verify the low degree of crystallinity of the as-prepared CoFe PBAs during such a rapid coordination polymerization process under normal pressure and temperature conditions, which is in accord with the SAED pattern (Fig. 2d). However, the diffraction peaks

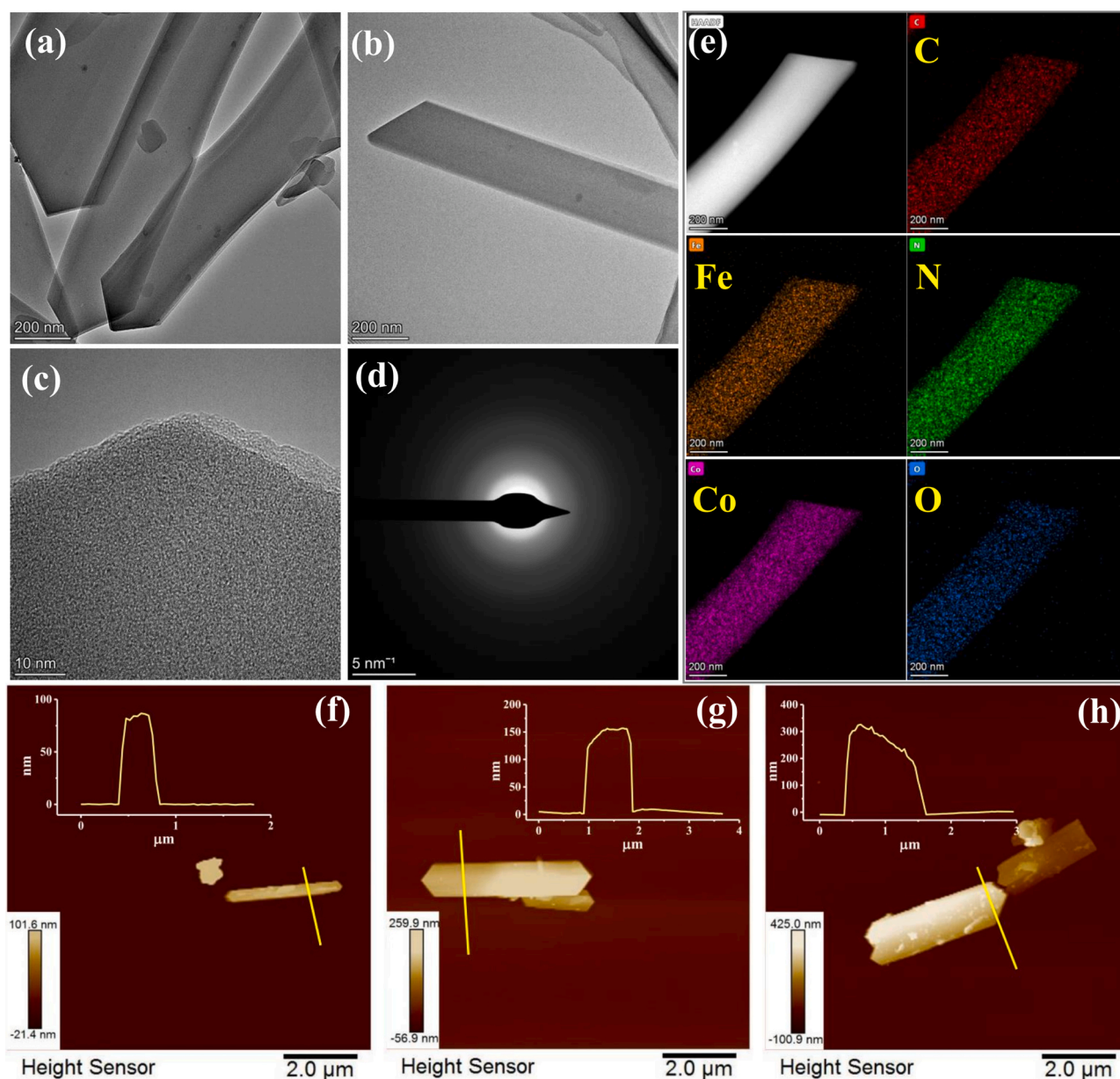


Fig. 2. (a–c) TEM images, (d) SAED pattern and (e) EDS mapping of CoFe PBAs-1 nanosheets; AFM images and thicknesses of (f) CoFe PBAs-1, (g) CoFe PBAs-2, and (h) CoFe PBAs-4.

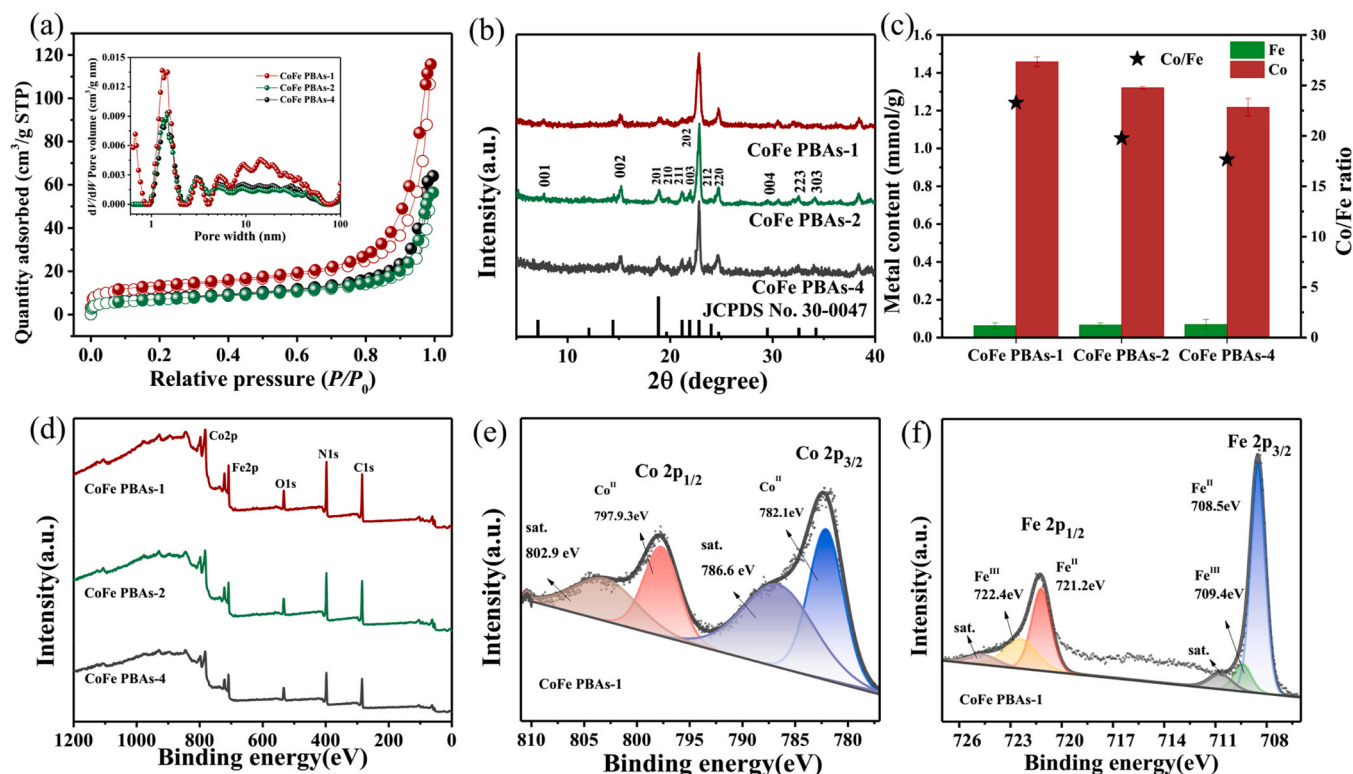


Fig. 3. (a) N_2 adsorption-desorption curves and pore distribution curves, (b) XRD patterns, (c) metal element content and Co/Fe ratio, and (d) XPS spectra for CoFe PBAs-1, CoFe PBAs-2 and CoFe PBAs-4; High-resolution XPS spectra of (e) Co 2p and (f) Fe 2p for CoFe PBAs-1.

indexed to the (001), (002), (201), (210), (211), (003), (202), (212), (220), (004), (223), and (303) planes are consistent with a standard $Co_2Fe(CN)_6$ compound (JCPDS No. 30-0047) [39], where Co^{II} is simultaneously located in the octahedral cavity of carbon ($C\equiv N$) and in the internal space of the crystallite unit cell as a charge-balancing ion. Based on the metal content measurement (Fig. 3c), it can be seen that the molar content of Co is significantly higher than that of Fe in the three samples, and the Co content decreased from CoFe PBAs-1 to CoFe PBAs-4, leading to a Co/Fe ratio declining from 23.3 of CoFe PBAs-1 to 19.8 of CoFe PBAs-2 and 17.6 of CoFe PBAs-4, much higher than the ratio of supplying precursor ions.

Both Co and Fe exist in the form of reduced states (Co^{II} and Fe^{II}) in the precursor ions supplied for constructing the PBA framework in this study, and XPS spectra are used to perform a deep analysis of the two transition metal elements (Fig. 3d). From the peak-differentiating and fitting results shown in Fig. 3e-f and Fig. S3, it can be observed that Co is relatively stable and remains in the Co^{II} state, while Fe undergoes partial oxidation during the coordination process. The XPS peaks located at 709.4 eV and 722.4 eV are assigned to $Fe\ 2p_{3/2}$ and $Fe\ 2p_{1/2}$ of Fe^{III} [40], demonstrating the conversion of a small amount of Fe^{II} to Fe^{III} in the coordination compound of CoFe PBA. Comparing the high-resolution XPS spectra for the Co/Fe elements, we find no significant difference for the three CoFe PBA samples prepared with different Co^{II}/Fe^{II} ratios. Thus, the control of the precursor ion ratio (Co^{II}/Fe^{II}) successfully enables the fabrication of a long-range and macroscopically periodic self-assembled structure, which can modify the 2D lamellar morphology (including its radial size and thickness) without affecting the chemical states of the transition metals in the frameworks.

3.2. Catalytic performance of the CoFe PBA sheets for norfloxacin degradation

The catalytic performance of the as-prepared CoFe PBA sheets was evaluated for antibiotic norfloxacin (NOR) degradation in a PMS-driven

bulk aqueous oxidation system, and the results are displayed in Fig. 4a. CoFe PBAs-1 presents an excellent catalytic capacity for NOR removal and can show complete degradation of NOR within 6 min after the addition of PMS oxidant, possessing a remarkably superior performance compared to that of CoFe PBAs-2 and CoFe PBAs-4 sheets. The catalytic rate constant ($k_1 = 0.773$) of CoFe PBAs-1 is nearly 4 times that of CoFe PBAs-2 ($k_2 = 0.204$) and CoFe PBAs-4 ($k_4 = 0.196$), as fitted from the quasi-first-order dynamic model shown in Fig. 4b. Therefore, the fabricated CoFe PBA sheets with smaller sizes, thinner lamellar and higher Co/Fe ratio (i.e., CoFe PBAs-1) lead to a superior catalytic performance because they have a higher surface area and enable more active sites to be exposed on the 2D sheet surface. The CoFe PBA sheets fabricated by the orientated growth of Prussian white crystals in this work can meet the dual-function requirement for constructing 2D catalytic membranes, i.e., i) serving as 2D building blocks for membrane assembly and ii) serving as active catalysts for organic contamination degradation.

3.3. Assembly and dynamic catalytic performance of 2D CoFe PBA catalytic membranes

A method of gas-pressing filtration was adopted to fabricate 2D catalytic membranes. CoFe PBA powder was first prepared into a dispersion aqueous solution under a 2 min ultrasound-assisted process. Then, the preparation of catalytic membranes was simply realized by the gas-pressing filtration of the CoFe PBA solution, as shown in Fig. 5a. A typical photograph of the as-prepared CoFe PBA catalytic membrane is displayed in Fig. 5b, which can be easily detached from the underlying substrate membrane to obtain a free-standing membrane, indicating a strong interaction force between the CoFe PBA sheets. The SEM images shown in Fig. 5c-e show the surface and interior morphologies of the assembled catalytic membrane. A flat interweaving network can be observed on the surface of the CoFe PBA catalytic membrane (Fig. 5c), which is different from the smooth and seamless surface observed for

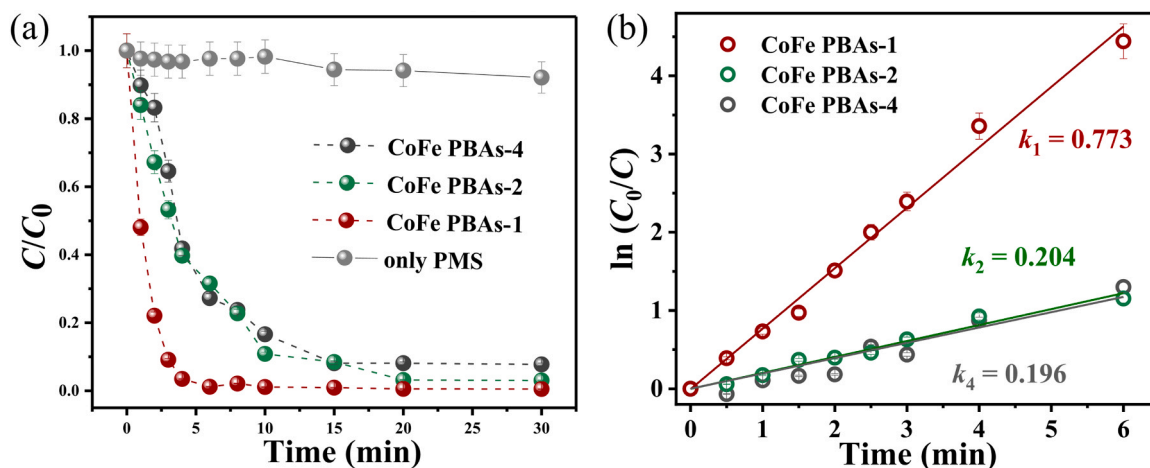


Fig. 4. (a) Catalytic performance of the three CoFe PBA powder samples for NOR degradation and (b) the corresponding fitting curves obtained using a quasi-first-order dynamic model (NOR concentration: 10 mg L^{-1} ; catalyst: $10 \text{ mg}/100 \text{ mL}$; PMS: 50 mg L^{-1}).

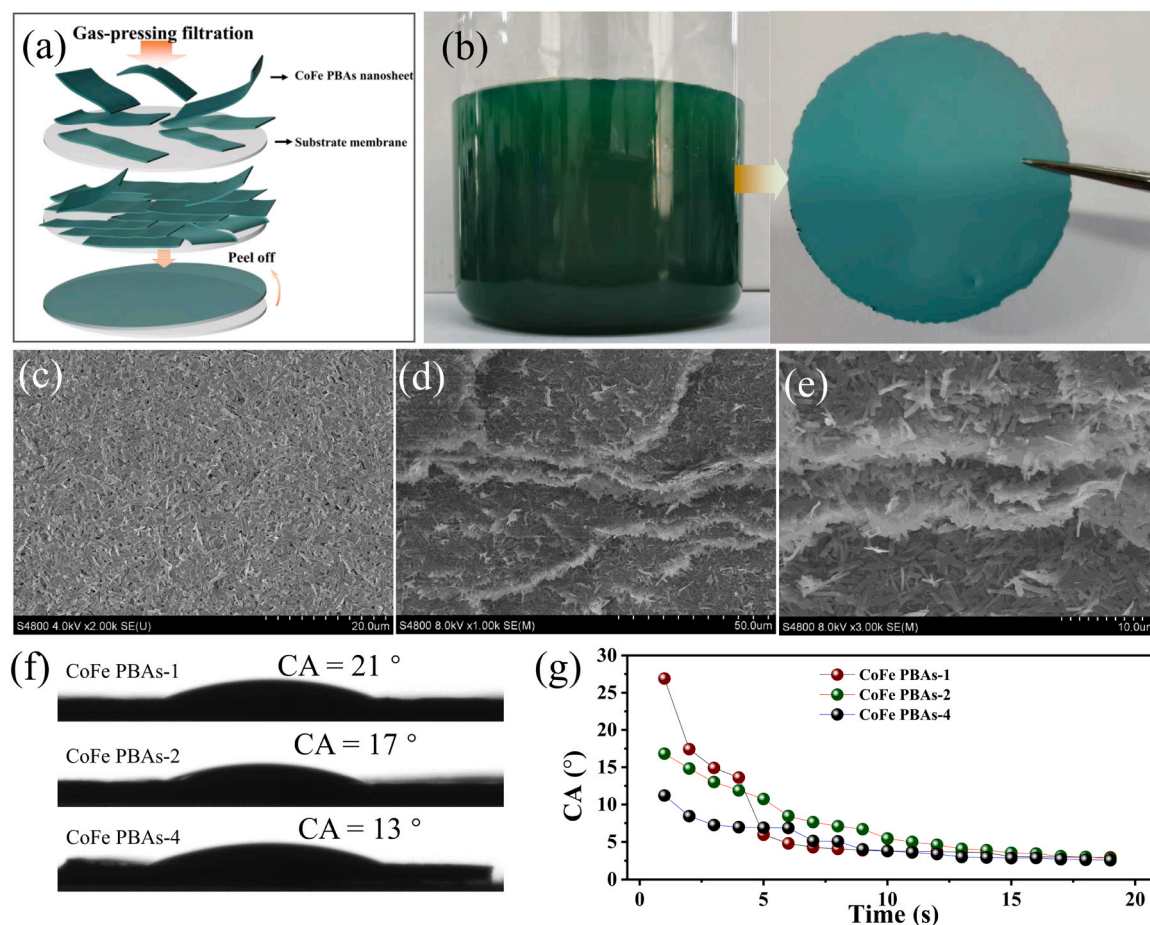


Fig. 5. (a) Schematic illustration of the assembly procedure for the free-standing CoFe PBA catalytic membrane; (b) photograph showing a free-standing CoFe PBA catalytic membrane; (c-e) SEM images of the surface and interior of the catalytic membrane; (f) instantaneous water contact angle and (g) variation in the dynamic water contact angle for the surfaces of the three CoFe PBA catalytic membranes.

other 2D membranes assembled from typical 2D nanosheets (such as graphene oxides, MoS_2 , and MXene) [41–43]. Given the insight into the interior of the catalytic membrane shown in Fig. 5d-e, the interlaced state of the blade-shaped sheets is much more obvious, which is more similar to the interweaving assembly of one-dimensional nanofibers than the orderly layer stacking of two-dimensional nanosheets. The stripe CoFe PBA sheets with a large length-width ratio leads to them to

behave more like one-dimensional materials; thus, their interweaving assembly leads to a strong interaction between building blocks and enables the free-standing property of the resultant catalytic membrane.

The hydrophilic-hydrophobic property of the fabricated CoFe PBA catalytic membranes was characterized by measuring their water contact angles. The ultralow initial static water contact angles (CA, $13\text{--}21^\circ$) of the membrane surface, as presented in Fig. 5f, illustrate a strongly

hydrophilic property, and CoFe PBAs-1 with a smaller sheet size leads to a slightly higher CA for the assembled catalytic membrane. The dynamic water CA variation curves shown in Fig. 5 g further reveal the superior wettability of the CoFe PBA membrane, which can achieve complete infiltration of a water drop within 15 s. Therefore, the excellent hydrophilic surface and superior wettability of the assembled CoFe PBA catalytic membrane can guarantee an unimpeded mass transfer process during the membrane catalysis process.

A homemade membrane catalytic setup with gas-pressing filtration was used to examine the dynamic membrane catalytic performance of the CoFe PBA membranes, as presented in Fig. 6a. The assembled CoFe PBA catalytic membrane was fixed in a stainless-steel membrane cell (Fig. 6b), and an aqueous solution containing the antibiotics NOR and PMS was continuously loaded and flowed through the membrane cell to realize dynamic catalytic degradation. The three CoFe PBA catalytic membranes are found to exhibit excellent instantaneous catalytic capacity for NOR, as shown in Fig. 6c, and the substrate membrane (hydrophilic mixed fiber membrane) makes little contribution to the removal of NOR. The CoFe PBAs-1 catalytic membrane can be used to achieve high instantaneous removal of NOR above 90 % during the first half hour of operation, which can still remain above 85 % even under continuous operation for 1 h, and the minor dissolution of metal ions (Fig. S4) during dynamic membrane catalysis might account for the slight decrease in catalytic efficiency. Such issue of metal ions dissolution is also a common problem faced by other metal-based catalysts, which can be alleviated by extending the coordination polymerization time to improve the crystallinity of CoFe PBA. The superwetting property of the assembled CoFe PBA catalytic membranes, as illustrated in

Fig. 5 g, is crucial for realizing such instantaneous catalysis because only the rapid contact of the flowing NOR and PMS can trigger the oxidation reaction and enable instantaneous catalysis performance. While, a hydrophobic or mild-hydrophilic membrane cannot realize such high-efficient instantaneous catalysis due to the mass transfer resistance and inadequate contact. In addition, the CoFe PBAs-1 catalytic membrane can achieve a relatively high water flux of $91.0 \text{ L m}^{-2} \text{ h}^{-1}$ at a very low operating pressure of 0.3 bar and shows weak flux attenuation after long-term operation (Fig. 6d), verifying its stable mass transfer channels that enable a stable membrane catalytic performance. The low-pressure operation characteristic highlights the low energy consumption advantage of this catalytic membrane. Although CoFe PBAs-2 and CoFe PBAs-4 catalytic membranes assembled from larger blade-shaped 2D sheets show larger water fluxes, their catalytic efficiency is decreased significantly. In particular, the decline in NOR removal is more significant on the CoFe PBAs-4 catalytic membrane during the continuous-running process, which can only maintain a removal efficiency of approximately 50 %. It's thought the higher water flux caused a short duration time for the NOR and PMS in the membrane pore of CoFe PBAs-4, which in turn led to a lower catalytic efficiency.

The stability of the mass transfer channels was further examined by a compaction resistance test under different operation pressures, as displayed in Fig. 7a. When the operation pressure is increased from 0.3 to 0.5 bar, the initial flux is slightly increased from 90.1 to $93.6 \text{ L m}^{-2} \text{ h}^{-1}$, which is calculated to have a similar permeance of $303 \text{ L m}^{-2} \text{ h}^{-1} \text{ bar}^{-1}$, and a decline in permeance of approximately 13.4 % (Fig. 7b) occurs after one hour of operation, illustrating the stable interior channel of the as-prepared catalytic membrane when running under low-pressure

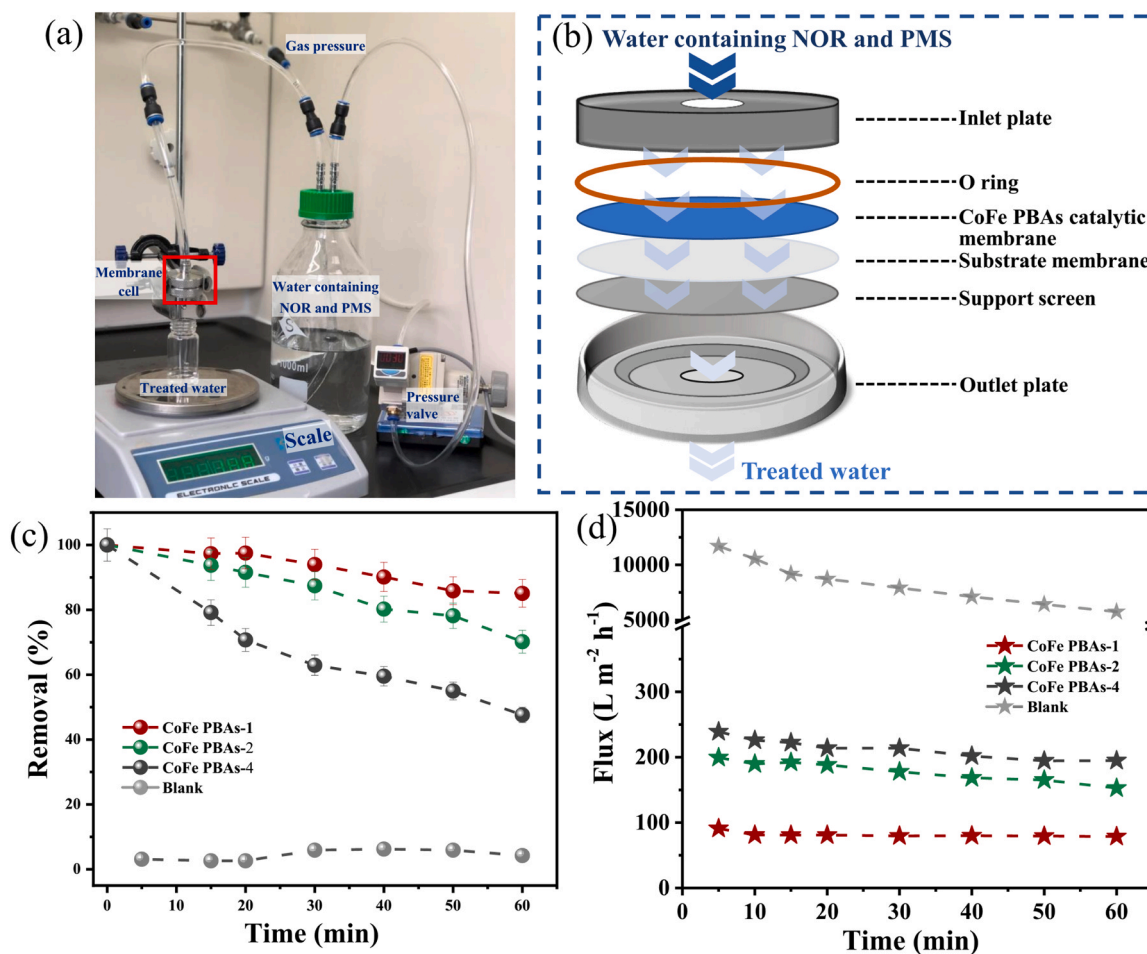


Fig. 6. (a) Photograph of the homemade gas-pressing filtration setup; (b) schematic representation of the configuration of the membrane cell; (c) removal efficiency and (d) flux for the three CoFe PBA catalytic membranes for NOR (NOR concentration: 10 mg L^{-1} ; pressure: 0.3 bar; PMS: 50 mg L^{-1}).

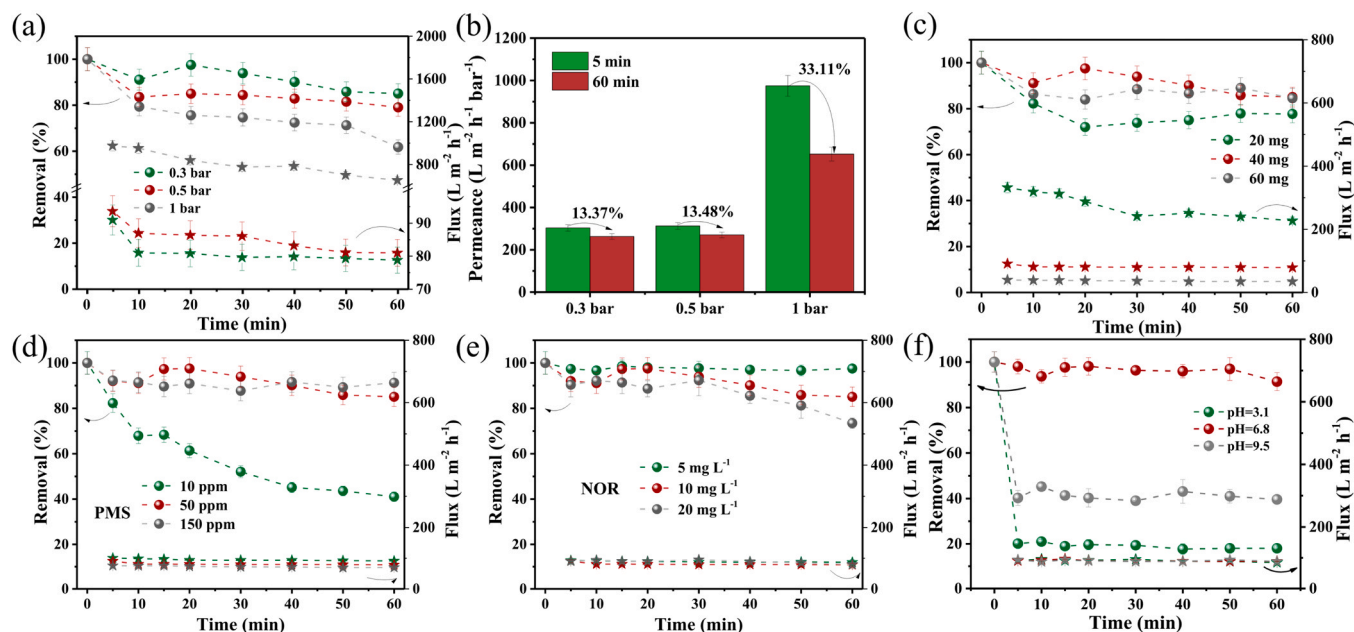


Fig. 7. (a) Catalytic membrane performance of CoFe PBAs-1 for the dynamic degradation of NOR under different pressures and (b) their corresponding permeance changes during 1 h operation (NOR concentration: 10 mg L^{-1} ; PMS: 50 mg L^{-1}). Catalytic membrane performance of CoFe PBAs-1 for the dynamic degradation under (c) different dosages of CoFe PBAs-1 nanosheets for membrane assembly, (d) different dosages of PMS and (e) different concentrations of NOR, at 0.3 bar; (f) different solution pH. (NOR concentration: 10 mg L^{-1} ; PMS: 50 mg L^{-1} ; at 0.3 bar).

conditions. However, as the operation pressure is further increased to 1 bar, the initial water flux is sharply increased to $974.6 \text{ L m}^{-2} \text{ h}^{-1}$, and the permeance is increased three times compared with that at low-pressure conditions (0.3 bar and 0.5 bar). The anomalous change in the permeance of the CoFe PBAs-1 catalytic membrane under relatively high-pressure conditions reflects deformation of the original channel in the membrane, which also leads to a remarkable decline in NOR degradation (Fig. 7a). Although the initial permeability is high, the permeance attenuation (33.1 %) is also very serious at 1 bar (Fig. 7b). Thus, these membranes represent a class of catalytic membranes suitable for low-pressure operation.

The effects of the amount of CoFe PBA sheets, PMS dosage and NOR concentration on membrane catalytic performance were further evaluated, and the results are displayed in Fig. 7c–e. A higher dosage of CoFe PBA sheets as building blocks for catalytic membrane assembly allows for a lower water flux due to the higher membrane thickness and longer mass transfer path. Correspondingly, increasing the CoFe PBA sheet loading can provide sufficient catalytic sites and extend the retention time for NOR and PMS in the channels; thus, the instantaneous NOR removal rate is relatively higher (above 85 % after 1 h of operation). Too low of a PMS dosage (10 mg L^{-1}) can limit the production of reactive species for NOR degradation, thus leading to a very poor catalytic performance (Fig. 7d), and the NOR removal rate is rapidly decreased to 67.8 % within 10 min and further decreased to 41.0 % after 1 h. When the PMS dosage is increased to 50 mg L^{-1} , the CoFe PBA catalytic membrane maintain a high removal rate for NOR degradation.

It's known that increasing PMS amount can cause the generation of more reactive oxygen species to attack organic pollutant. However, further increasing the PMS dosage to 150 mg L^{-1} does not lead to a further improvement in the catalytic performance. Although it's reported that too much PMS will result in free radical consumption by itself and inhibit the catalytic efficiency [44], excessive PMS oxidant neither pushed the oxidation reaction forward nor inhibited the NOR degradation when the PMS dosage increased to 150 mg L^{-1} indicates that the degradation kinetics for NOR might be controlled by the dynamic flow rate rather than by the oxidation reaction in such cases. For the treatment of low-concentration NOR (5 mg L^{-1}), CoFe PBA catalytic

membrane was able to maintain a consistently high removal rate of over 96 % throughout the entire 1 h operation (Fig. 7e). While, for high-concentration NOR (20 mg L^{-1}), it can exhibit superior catalytic efficiency (above 90 %) during the first half hour of dynamic catalytic process, which was then followed by a significant decline of the catalytic capacity with a removal rate of 73 % after 1 h running. Therefore, the CoFe PBA/PMS catalytic system should be an ideal oxidation system to degrade low-concentration antibiotic pollutants. Both of PMS dosage and NOR concentration significantly affected the catalytic efficiency, but had little effect on the membrane flux. Solution pH is a critical factor that affecting the catalytic process, which not only determined the existence forms of PMS ($\text{pK}_a = 9.4$) and NOR ($\text{pK}_{a1} = 6.2$, $\text{pK}_{a2} = 8.5$) but also dominated the surface charge of the catalytic membrane. Thus, the effect of solution pH on the catalytic efficiency was examined for the CoFe PBA catalytic membrane. The results in Fig. 7f show that acidic ($\text{pH} = 3.1$) or alkaline ($\text{pH} = 9.5$) condition would inhibit the membrane catalytic efficiency, especially the acidic condition, the inhibition effect was more significant and the NOR removal rate was only ~20 %. For all this, the membrane flux was not affected by solution pH. So, the catalytic membrane is suitable for treating neutral wastewater.

The degradation products of NOR after instantaneous catalysis using CoFe PBA membrane were identified using Q-TOF mass spectra, and the results in Fig. 8a shows a near-complete mineralization of NOR (with m/z of 320) that almost no intermediates were detected. Furthermore, a continuous dynamic catalytic test lasting 10 h was conducted to assess the operational stability of the assembled CoFe PBA catalytic membrane for NOR removal. The result in Fig. 8b further verifies the superior stability of interior transfer channel of the catalytic membrane under low-pressure operation which kept a relatively stable water flux ($77.0 \text{ L m}^{-2} \text{ h}^{-1}$, calculated to a permeance of $256.7 \text{ L m}^{-2} \text{ h}^{-1} \text{ bar}^{-1}$) after 10 h of continuous flow-through catalysis, only with a 14.6 % decline compared with its initial flux. The removal rate of NOR (10 mg L^{-1}) remained above 85 % in 5 h, but then the attenuation became obvious, and the removal rate gradually declined to 71.7 % after 10 h. Therefore, a progressive loss of catalytic efficiency should be considered and overcome in a long-term application of the dynamic catalytic membrane. The chemical stability of the CoFe PBA catalytic

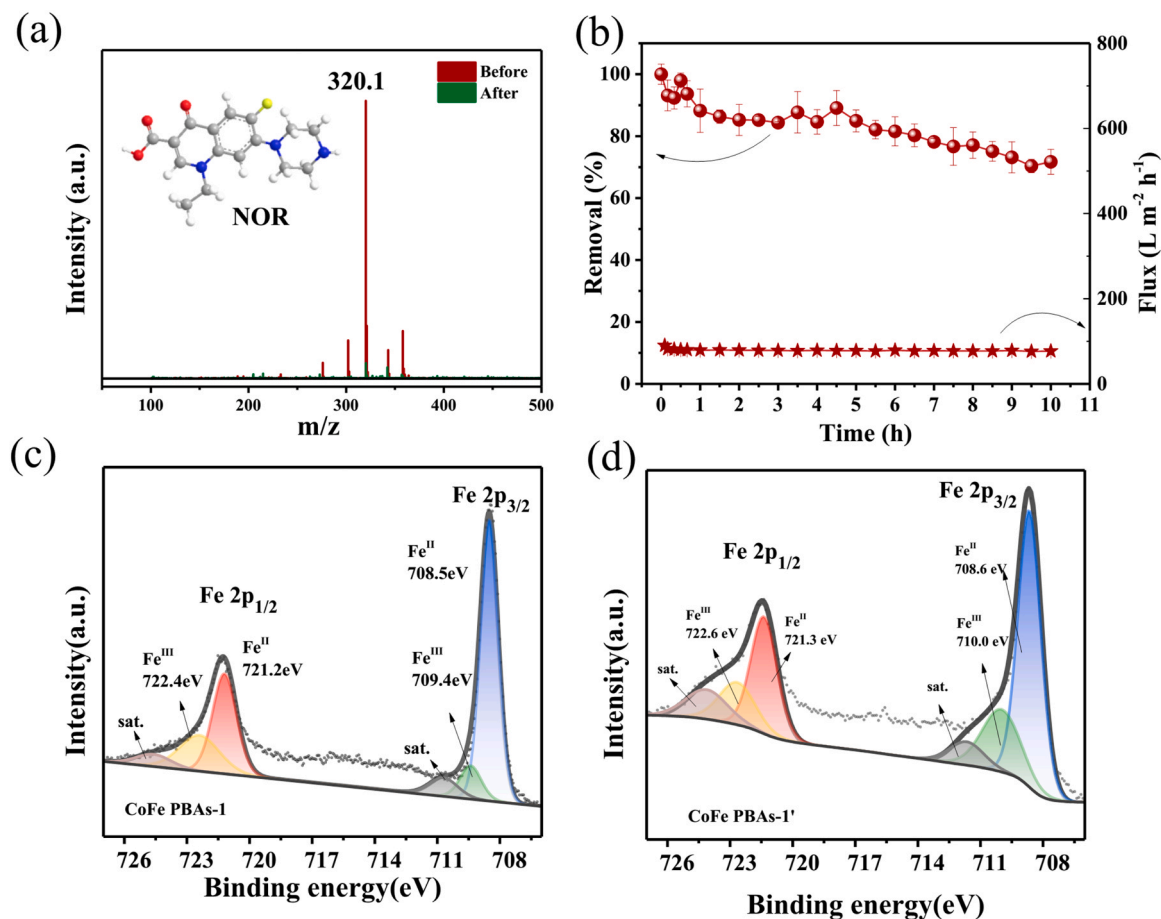


Fig. 8. (a) Q-TOF mass spectra of NOR before and after membrane catalysis; (b) Long-term test of the performance of CoFe PBAs-1 catalytic membrane (NOR concentration: 10 mg L⁻¹; PMS: 50 mg L⁻¹; at 0.3 bar); High-resolution XPS spectra of Fe 2p for CoFe PBAs-1 catalytic membrane (c) before and (d) after reaction.

membrane after long-term catalysis application was examined by XPS analysis. As shown in Fig. 8c-d and S5, Co maintained a relatively stable chemical valent state of Co^{II} with Co 2p_{3/2} located at 782.0 eV and Co 2p_{1/2} located at 797.7 eV even after a long-term of PMS oxidation, while which was different observed on Fe. It can be compared for Figs. 8c and 8d that the XPS peaks at 710.0 eV and 722.6 eV assigned to the 2p_{3/2} and 2p_{1/2} of Fe^{III} increased significantly after catalysis, resulting in an increase of the Fe^{III} content from 20.6 % to 25.6 %. It means that partial Fe^{II} in CoFe PBA was irreversibly oxidized to Fe^{III} during the long-term membrane catalytic process, and this can properly account for the progressive decline of catalytic efficiency in Fig. 8b.

3.4. Activation mechanism for PMS for NOR degradation during the dynamic catalytic process

The assembled CoFe PBA catalytic membrane exhibits excellent instantaneous catalytic capacity for NOR during a continuous dynamic membrane process, and the catalytic mechanisms for PMS activation for NOR degradation were further studied. It's known that the metals of Fe^{II} and Co^{II} in the coordination frameworks of CoFe PBA sheets provided the main active sites for the PMS activation to generate reactive species, and a continuous NOR degradation was facilitated by the redox pair cycles of Fe^{II}/Fe^{III} and Co^{II}/Co^{III}. EPR experiments were carried out using DMPO and TEMP as spin-trapping agents, which is a reliable method for the in-situ detection of reactive radical species [45]. As shown in Fig. 9a, no obvious signals can be observed in the EPR spectra measured for DMPO-•OH/SO₄^{•-}, indicating that •OH and SO₄^{•-} are not detected in the PMS+DMPO+CoFe PBAs-1 system [46]. As opposed to the above observation, the characteristic signals with an intensity ratio

of 1:2:1:2:1:2:1 are captured, which are assigned to nitroxide radicals of DMPO (5,5-dimethylpyrroline-(2)-oxyl-(1); DMPOX). It has been reported that the DMPOX signal can be generated via SO₄^{•-}-induced oxidation of DMPO because the DMPO-SO₄ adduct has lower sensitivity and is unstable and can be immediately transformed to DMPOX [47,48]. In addition, no signals are detected for DMPO-•O₂⁻ when using DMPO as the spin-trapping agent [49]. Fig. 9b displays the TEMP-¹O₂ spectra, and the standard 1:1:1 triple signal assigned to ¹O₂ can be clearly observed in the PMS+DMPO+CoFe PBAs-1 system, indicating that ¹O₂ can be the main generated reactive species.

To determine the reactive species responsible for NOR degradation, radical quenching experiments were conducted. Methanol (MeOH) can scavenge both SO₄^{•-} ($k_{SO_4^{\bullet-}} = 3.2 \times 10^6 \text{ M}^{-1}\text{s}^{-1}$) and •OH ($k_{\bullet OH} = 9.7 \times 10^8 \text{ M}^{-1}\text{s}^{-1}$), while the scavenging capacity of tert-butanol (TBA) for •OH ($k_{\bullet OH} = 5.2 \times 10^8 \text{ M}^{-1}\text{s}^{-1}$) is obviously higher than that of SO₄^{•-} ($k_{SO_4^{\bullet-}} = 8.4 \times 10^5 \text{ M}^{-1}\text{s}^{-1}$) [50,51]; thus, TBA can serve as a quenching agent for •OH. As shown in Fig. 9c, the degradation process is unaffected by the introduction of TBA, revealing the negligible role of •OH for NOR degradation, while the addition of MeOH leads to a remarkable inhibition effect on NOR degradation. This result is consistent with the above EPR spectra that SO₄^{•-} rather than •OH is generated in the PMS-driven NOR degradation using the CoFe PBAs-1 catalyst. L-histidine was used as the quenching agent of ¹O₂, which almost completely inhibited NOR degradation. It's known that when L-histidine quenches ¹O₂, it will also consume a lot of PMS. Therefore, we further carried out a test of the effect of Cl⁻ on the catalytic performance, to clarify the contribution of SO₄^{•-} and ¹O₂, because Cl⁻ can consume radicals and be converted to •Cl and Cl₂^{•-} radicals with lower redox potentials, subsequently suppressing the catalytic efficiency, while it has

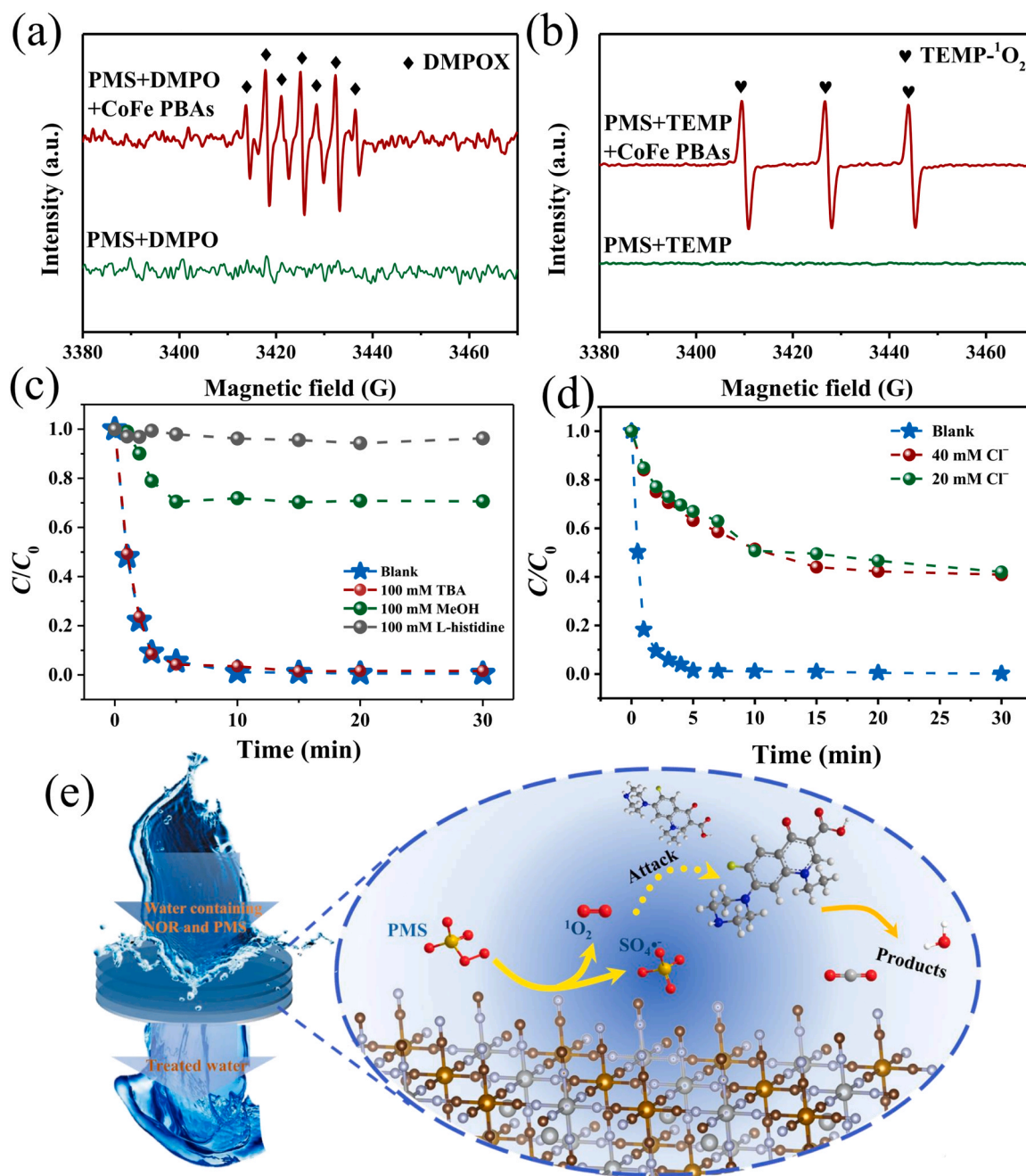


Fig. 9. EPR spectra measured for (a) DMPOX and (b) TEMP- $^1\text{O}_2$ adducts in the CoFe PBAs-1/PMS system; (c) NOR degradation curves obtained for CoFe PBAs-1 in the presence of various quenching agents; (d) Effect of Cl^- on NOR degradation by CoFe PBAs-1; (e) Schematic illustration of the dynamic catalysis mechanism occurring in the CoFe PBA membrane for NOR degradation.

a negligible impact on $^1\text{O}_2$ [52]. Fig. 9d shows that Cl^- had a quite significant inhibitory effect on NOR degradation, but the inhibitory effect did not increase with the increase of Cl^- concentration. Nearly 50 % of the removal rate was retained, which can be ascribed to the nonradical pathway. These results reveal that the radical pathway of $\text{SO}_4^{\bullet-}$ and the nonradical pathway of $^1\text{O}_2$ activated by CoFe PBA sheets are the two dominant oxidation pathways (Fig. 8e), which can lead to synergistic attack of organic pollutants during the dynamic membrane catalysis process.

4. Conclusions

2D blade-shaped CoFe Prussian blue analog (PBA) sheets were successfully fabricated on a large scale by restricting the growth of the

coordination polymer in one direction at room temperature without the use of any template reagent, exfoliation step or harsh conditions. The radial size and thickness of CoFe PBA sheets can be adjusted by the precursor ion ratio ($\text{Co}^{\text{II}}/\text{Fe}^{\text{II}}$), and the use of a high $\text{Co}^{\text{II}}/\text{Fe}^{\text{II}}$ ratio can lead to a smaller sheet size, smaller lamellar thickness and higher specific surface area for the CoFe PBA sheets. The as-prepared CoFe PBA sheets can be simply assembled into a free-standing membrane via gas-pressing filtration, and the stripe CoFe PBA sheets with a large length-width ratio leads to an interweaving assembly within the membrane, similar to that for one-dimensional materials. The assembled CoFe PBA catalytic membrane presents an excellent hydrophilic surface and superior wetting property, which guarantees an unimpeded mass transfer process and excellent instantaneous catalytic performance. The dynamic removal for antibiotic NOR is maintained above 85 %, and the water flux

is maintained at a stable level (with an initial value of $91.0 \text{ L m}^{-2} \text{ h}^{-1}$, at 0.3 bar) during the continuous-running and flow-through membrane catalysis process. The operation pressure, building block amount and PMS dosage can significantly affect the membrane catalytic capacity, and the CoFe PBA catalytic membrane is proven to be suitable for low-pressure operation, representing a new type of catalytic membrane with low energy consumption. EPR spectra and radical quenching tests verify that $\text{SO}_4^{\cdot-}$ and $^1\text{O}_2$ are synergistically activated by the CoFe PBA building blocks and contribute to PMS-driven organic degradation during the flow-through membrane catalytic process.

CRedit authorship contribution statement

Jiaxin Li: Investigation, Writing – original draft. **Huiyu Yi:** Investigation, Formal analysis, Validation. **Yang Xiao:** Validation, Writing – review & editing. **Chenge Liang:** Investigation, Validation. **Yi Shen:** Writing – review & editing, Funding acquisition. **Yungui Li:** Validation, Visualization, Funding acquisition. **Qile Fang:** Conceptualization, Writing – original draft, Writing – review & editing, Supervision, Visualization, Funding acquisition.

Declaration of Competing Interest

The authors declare that they have no known competing financial interests or personal relationships that could have appeared to influence the work reported in this paper.

Data availability

Data will be made available on request.

Acknowledgements

This work was kindly supported by Zhuhai Basic and Applied Basic Research Foundation (ZH22017003210025PWC); Special Projects in Key Areas of Ordinary Universities of Department of Education of Guangdong Province (2022ZDZX4064); the startup fund to Qile Fang from Advanced Institute of Natural Sciences, Beijing Normal University at Zhuhai; Sichuan Science and Technology Program (2021YFH0046); National Natural Science Foundation of China (22006131).

Appendix A. Supporting information

Supplementary data associated with this article can be found in the online version at [doi:10.1016/j.apcatb.2023.122922](https://doi.org/10.1016/j.apcatb.2023.122922).

References

- H.Y. Kim, J. Asselman, T.-Y. Jeong, S. Yu, K.A.C.D. Schampelaere, S.D. Kim, Multigenerational effects of the antibiotic tetracycline on transcriptional responses of *Daphnia magna* and its relationship to higher levels of biological organizations, *Environ. Sci. Technol.* 51 (2017) 12898–12907.
- O. Jovanovic, C.F. Amabile-Cuevas, C. Shang, C. Wang, K.W. Ngai, What water professionals should know about antibiotics and antibiotic resistance: an overview, *ACS EST Water* 1 (2021) 1334–1351.
- F. Polesel, H.R. Andersen, S. Trapp, B.G. Plosz, Removal of antibiotics in biological wastewater treatment systems – a critical assessment using the activated sludge modeling framework for Xenobiotics (ASM-X), *Environ. Sci. Technol.* 50 (2016) 10316–10334.
- B.C. Hodges, E.L. Cates, J.-H. Kim, Challenges and prospects of advanced oxidation water treatment processes using catalytic nanomaterials, *Nat. Nanotechnol.* 13 (2018) 642–650.
- J. Lee, U. Gunten, J.-H. Kim, Persulfate-based advanced oxidation: critical assessment of opportunities and roadblocks, *Environ. Sci. Technol.* 54 (2020) 3064–3081.
- N. Li, X. Lu, M. He, X. Duan, B. Yan, G. Chen, S. Wang, Catalytic membrane-based oxidation-filtration systems for organic wastewater purification: a review, *J. Hazard. Mater.* 44 (2021), 125478.
- J. Xie, Z. Liao, M. Zhang, L. Ni, J. Qi, C. Wang, X. Sun, L. Wang, S. Wang, J. Li, Sequential ultrafiltration-catalysis membrane for excellent removal of multiple pollutants in water, *Environ. Sci. Technol.* 55 (2021) 2652–2661.
- Z. Qiu, X. Xiao, W. Yu, X. Zhu, C. Chu, B. Chen, Selective separation catalysis membrane for highly efficient water and soil decontamination via a persulfate-based advanced oxidation process, *Environ. Sci. Technol.* 56 (2022) 3234–3244.
- H. Lin, Q. Fang, W. Wang, G. Li, J. Guan, Y. Shen, J. Ye, F. Liu, Prussian blue/PVDF catalytic membrane with exceptional and stable Fenton oxidation performance for organic pollutants removal, *Appl. Catal. B Environ.* 273 (2020), 119047.
- D.M. Dotzauer, J. Dai, L. Sun, M.L. Bruening, Catalytic membranes prepared using layer-by-layer adsorption of polyelectrolyte/metal nanoparticle films in porous supports, *Nano Lett.* 6 (2006) 2268–2272.
- S. Zhang, M. Sun, T. Hedtke, A. Deshmukh, X. Zhou, S. Weon, M. Elimelech, J.-H. Kim, Mechanism of heterogeneous Fenton reaction kinetics enhancement under nanoscale spatial confinement, *Environ. Sci. Technol.* 54 (2020) 10868–10875.
- C. Yu, Z. Xiong, H. Zhou, P. Zhou, H. Zhang, R. Huang, G. Yao, B. Lai, Marriage of membrane filtration and sulfate radical-advanced oxidation processes (SR-AOPs) for water purification: current developments, challenges and prospects, *Chem. Eng. J.* 433 (2022), 133802.
- C. Meng, B. Ding, S. Zhang, L. Cui, K.K. Ostrikov, Z. Huang, B. Yang, J.-H. Kim, Z. Zhang, Angstrom-confined catalytic water purification within Co-TiOx laminar membrane nanochannels, *Nat. Commun.* 13 (2022) 4010.
- Y. Chen, G. Zhang, H. Liu, J. Qu, Confining free radicals in close vicinity to contaminants enables ultrafast Fenton-like processes in the interspace of MoS₂ membranes, *Angew. Chem. Int. Ed.* 58 (2019) 8134–8138.
- C. Meng, Z. Wang, W. Zhang, L. Cui, B. Yang, H. Xie, Z. Zhang, Laminar membranes assembled by ultrathin cobalt-copper oxide nanosheets for nanoconfined catalytic degradation of contaminants, *Chem. Eng. J.* 449 (2022), 137811.
- J. Wei, J. Bi, L. Zhang, D. Han, J. Gong, Gravity-driven Fe-doped CoTiO₃/SiO₂ fiber membrane with open catalytic network: activation of peroxymonosulfate and efficient pollutants removal, *Sep. Purif. Technol.* 280 (2022), 119975.
- Y. Yang, W. Fu, X. Chen, L. Chen, C. Hou, T. Tang, X. Zhang, Ceramic nanofiber membrane anchoring nanosized Mn₂O₃ catalytic ozonation of sulfamethoxazole in water, *J. Hazard. Mater.* 436 (2022), 129168.
- M. Zhao, Y. Wang, Q. Ma, Y. Huang, X. Zhang, J. Ping, Z. Zhang, Q. Lu, Y. Yu, H. Xu, Y. Zhao, H. Zhang, Ultrathin 2D metal-organic framework nanosheets, *Adv. Mater.* 27 (2015) 7372–7378.
- A. Dhakshinamoorthy, A.M. Asiri, H. Garcia, 2D metal-organic frameworks as multifunctional materials in heterogeneous catalysis and electro/photocatalysis, *Adv. Mater.* (2019), 1900617.
- M.B. Asif, H. Kang, Z. Zhang, Gravity-driven layered double hydroxide nanosheet membrane activated peroxymonosulfate system for micropollutant degradation, *J. Hazard. Mater.* 425 (2022), 127988.
- L.-L. Liu, J. Chen, Y. Zhang, C.-X. Yu, W. Du, X.-Q. Sun, J.-L. Zhang, F.-L. Hu, Y. Mi, L.-F. Ma, Fabrication of ultrathin single-layer 2D metal-organic framework nanosheets with excellent adsorption performance via a facile exfoliation approach, *J. Mater. Chem. A* 9 (2021) 546–555.
- M. Jian, R. Qiu, Y. Xia, J. Lu, Y. Chen, Q. Gu, R. Liu, C. Hu, J. Qu, H. Wang, X. Zhang, Ultrathin water-stable metal-organic framework membranes for ion separation, *Sci. Adv.* 6 (2020), eaay3998.
- X. Yu, Z. Liu, Z. Zhu, H. Luo, Controllable construction 2D-CN photocatalyst for degradation MBT and mechanism insights, *Mater. Res. Bull.* 159 (2023), 112093.
- F.-L. Li, P. Wang, X. Huang, D.J. Young, H.-F. Wang, P. Braunstein, J.-P. Lang, Large-scale, bottom-up synthesis of binary metal-organic framework nanosheets for efficient water oxidation, *Angew. Chem. Int. Ed.* 58 (2019) 7051–7056.
- S. Dai, F. Nour, S. Zhang, A. Tissot, C. Serre, One-step room-temperature synthesis of metal (IV) carboxylate metal-organic frameworks, *Angew. Chem. Int. Ed.* 60 (2021) 4282–4288.
- J. Nai, X.W. Lou, Hollow structures based on Prussian blue and its analogs for electrochemical energy storage and conversion, *Adv. Mater.* (2018), 1706825.
- Y. Pi, L. Ma, P. Zhao, Y. Cao, H. Gao, C. Wang, Q. Li, S. Dong, J. Sun, Facile green synthetic graphene-based Co-Fe Prussian blue analogues as an activator of peroxymonosulfate for the degradation of levofloxacin hydrochloride, *J. Colloid Interf. Sci.* 526 (2018) 18–27.
- F. Guo, K. Wang, J. Lu, J. Chen, X. Dong, D. Xia, A. Zhang, Q. Wang, Activation of peroxymonosulfate by magnetic carbon supported Prussian blue nanocomposite for the degradation of organic contaminants with singlet oxygen and superoxide radicals, *Chemosphere* 218 (2019) 1071–1081.
- T. Wi-Afedzi, E. Kwon, D.D. Tuan, K.-Y.A. Lin, F. Ghanbari, Copper hexacyanoferrate nanocrystal as a highly efficient non-noble metal catalyst for reduction of 4-nitrophenol in water, *Sci. Total Environ.* 703 (2020), 134781.
- C. Zhao, B. Liu, X. Li, K. Zhu, R. Hu, Z. Ao, J. Wang, A Co-Fe Prussian blue analogue for efficient Fenton-like catalysis: the effect of high-spin cobalt, *Chem. Commun.* 55 (2019) 7151.
- J. Liu, X. Li, B. Liu, C. Zhao, Z. Kuang, R. Hu, B. Liu, Z. Ao, J. Wang, Shape-controlled synthesis of metal-organic frameworks with adjustable Fenton-like catalytic activity, *ACS Appl. Mater. Interface* 10 (2018) 38051–38056.
- D. Aguilera, Y. Prado, E.S. Koumoussi, C. Mathoniere, R. Clerac, Switchable Fe/Co Prussian blue networks and molecular analogues, *Chem. Soc. Rev.* 45 (2016) 203–224.
- B. Kong, C. Selomulya, G. Zheng, D. Zhao, New faces of porous Prussian blue: interfacial assembly of integrated hetero-structures for sensing applications, *Chem. Soc. Rev.* 44 (2015) 7997–8018.
- J. Nai, X.W. Lou, Hollow structures based on Prussian blue and its analogs for electrochemical energy storage and conversion, *Adv. Mater.* (2018), 1706825.
- C.Q.X. Lim, Z. Tan, Prussian white with near-maximum specific capacity in sodium-ion batteries, *ACS Appl. Energy Mater.* 4 (2021) 6214–6220.
- Z. Xu, C. Gao, Aqueous liquid crystals of graphene oxide, *ACS Nano* 5 (2011) 2908–2915.

- [37] J.E. Kim, T.H. Han, S.H. Lee, J.Y. Kim, C.W. Ahn, J.M. Yun, S.O. Kim, Graphene oxide liquid crystals, *Angew. Chem. Int. Ed.* 50 (2011) 3043–3047.
- [38] W.-J. Li, C. Han, G. Cheng, S.-L. Chou, H.-K. Liu, S.-X. Dou, Chemical properties, structural properties, and energy storage applications of Prussian blue analogues, *Small* 15 (2019), 1900470.
- [39] T. Čeranić, The structure model of an inorganic ion exchanger cobalt(II)-hexacyanoferrate(II), *Z. Naturforsch.* 33b (1978) 1484–1488.
- [40] W. Wang, H. Wang, G. Li, P.K. Wong, T. An, Visible light activation of persulfate by magnetic hydrochar for bacterial inactivation: efficiency, recyclability and mechanisms, *Water Res.* 176 (2020), 115746.
- [41] G. Liu, W. Jin, N. Xu, Two-dimensional-material membranes: a new family of high-performance separation membranes, *Angew. Chem. Int. Ed.* 55 (2016) 13384–13397.
- [42] Y. Kang, Y. Xia, H. Wang, X. Zhang, 2D laminar membranes for selective water and ion transport, *Adv. Funct. Mater.* 29 (2019), 1902014.
- [43] Y. Chen, G. Zhang, H. Liu, J. Qu, Confining free radicals in close vicinity to contaminants enables ultrafast Fenton-like processes in the interspacing of MoS₂ membranes, *Angew. Chem. Int. Ed.* 58 (2019) 8134–8138.
- [44] J. Ye, J. Dai, C. Li, Y. Yan, Lawn-like Co₃O₄@N-doped carbon-based catalytic self-cleaning membrane with peroxydisulfate activation: a highly efficient singlet oxygen dominated process for sulfamethoxazole degradation, *Chem. Eng. J.* 421 (2021), 127805.
- [45] D. Ding, S. Yang, L. Chen, T. Cai, Degradation of norfloxacin by CoFe alloy nanoparticles encapsulated in nitrogen doped graphitic carbon (CoFe@N-GC) activated peroxydisulfate, *Chem. Eng. J.* 392 (2020), 123725.
- [46] P. Duan, J. Pan, W. Du, Q. Yue, B. Gao, X. Xu, Activation of peroxydisulfate via mediated electron transfer mechanism on single-atom Fe catalyst for effective organic pollutants removal, *Appl. Catal. B Environ.* 299 (2021), 120714.
- [47] S. Maeno, Q. Zhu, M. Sasaki, T. Miyamoto, M. Fukushima, Monopersulfate oxidation of tetrabromobisphenol A by an iron(III)-phthalocyaninetetrasulfate catalyst coordinated to imidazole functionalize silica particles, *J. Mol. Catal. A Chem.* 400 (2015) 56–63.
- [48] J. Du, J. Bao, Y. Liu, S.H. Kim, D.D. Dionysiou, Facile preparation of porous Mn/Fe₃O₄ cubes as peroxydisulfate activating catalyst for effective bisphenol A degradation, *Chem. Eng. J.* 376 (2019), 119193.
- [49] Z. Zhu, R. Kumar, L. Luo, S. Varjani, P. Huo, J.W.-C. Wong, J. Zhao, Quantum effect and Mo–N surface bonding states of α -MoC_{1-x} modified carbon nitride for boosting photocatalytic performance, *Catal. Sci. Technol.* 12 (2022) 6384–6397.
- [50] W. Wang, H. Wang, G. Li, T. An, H. Zhao, P.K. Wong, Catalyst-free activation of persulfate by visible light for water disinfection: efficiency and mechanisms, *Water Res.* 157 (2019) 106–118.
- [51] C. Zhu, L. Lu, Q. Fang, S. Song, B. Chen, Y. Shen, Unveiling spin state-dependent micropollutant removal using single-atom covalent triazine framework, *Adv. Funct. Mater.* (2023), 2210905.
- [52] C. Chen, T. Ma, Y. Shang, B. Gao, B. Jin, H. Dan, Q. Li, Q. Yue, Y. Li, Y. Wang, X. Xu, In-situ pyrolysis of Enteromorpha as carbocatalyst for catalytic removal of organic contaminants: considering the intrinsic N/Fe in Enteromorpha and non-radical reaction, *Appl. Catal. B Environ.* 250 (2019) 382–395.